Eur. Phys. J. C (2025) 85:441
https://doi.org/10.1140/epjc/s10052-025-14110-3

THE EUROPEAN PHYSICAL JOURNAL C

Check for updates

Regular Article - Theoretical Physics

Constraining the metric-affine bumblebee gravity parameter using black hole shadows and quasiperiodic oscillations of galactic microquasars

Sohan Kumar Jha[1,a], **Anisur Rahaman**[2,b]

[1] Chandernagore College, Chandernagore, Hooghly, West Bengal, India
[2] Department of Physics, Durgapur Government College, Durgapur, Burdwan, West Bengal 713214, India

Received: 21 December 2024 / Accepted: 23 March 2025
© The Author(s) 2025

Abstract We examine a static spherically symmetric black hole metric that originates from the vacuum solution of the traceless metric-affine bumblebee model in which spontaneous Lorentz symmetry-breaking occurs when the bumblebee fields acquire a non-vanishing vacuum expectation value. A free Lorentz-violating parameter enters into the basic formulation of the metric-affine bumblebee model. In this study, we use observations from the Event Horizon Telescope (EHT) collaboration on $M87^*$ and $SgrA^*$ to analyse the shadow of the black hole and an attempt has been made to constrain that free Lorentz-violating parameter. We also investigate particle motion over time-like geodesics and compute the corresponding epicyclic frequencies. We further constrain the Lorentz-violating parameter by using the reported high-frequency quasi-periodic oscillations (QPOs) of microquasars, offering new insights into its possible impact on astrophysical phenomena.

1 Introduction

In theoretical physics, the quest for a unified understanding of fundamental forces often lead to the introduction of free parameters that allow for flexibility in model formulation. Among these, the Lorentz symmetry-violating parameters are particularly significant. Lorentz symmetry, a cornerstone of both special relativity and the Standard Model of particle physics dictates that the laws of physics remain invariant under transformations such as rotations and boosts. However, theories that explore physics beyond the Standard Model, such as quantum gravity models and extensions of general relativity, often introduce parameters that could violate this symmetry [1–4].

Contracting these free parameters is crucial for several reasons. First, it helps in constraining the parameter space by aligning theoretical predictions with experimental observations. For instance, the Lorentz violation parameter can impact a range of physical phenomena, from the behavior of particles in high-energy collisions to the propagation of light in astrophysical contexts [5]. Second, understanding the bounds of such parameters aids in testing the robustness of theoretical frameworks against experimental data. By setting limits on the degree of Lorentz violation, we ensure that new theories remain consistent with well-established principles and empirical evidence.

In practical terms, contracting Lorentz symmetry-violating parameters are essential for refining theoretical models and guiding experimental searches. This process helps to validate or refute proposed theories while offering insights into the fundamental structure of spacetime, potentially signaling the need for new physics beyond the Standard Model [1–4].

In the context of black hole physics, investigating Lorentz violation becomes particularly compelling. Black holes provide a unique testing ground for probing fundamental physics in extreme gravitational environments. The introduction of Lorentz-violating parameters can lead to observable deviations in phenomena such as black hole shadows [6–9], Hawking radiation [10,11], and quasinormal modes (QNMs) [12–17] These deviations are critical as they help to constrain the magnitude of Lorentz violation by comparing theoretical predictions with astrophysical observations, such as the imaging of black hole shadows by EHT [6–9] or the analysis of gravitational waves from the black hole mergers [18].

[a] e-mail: sohan00slg@gmail.com
[b] e-mails: manisurn@gmail.com; anisur@associates.iucaa.in (corresponding author)

Published online: 21 April 2025

Black holes, arising as solutions to Einstein's equations, have long been at the center of understanding the nature of spacetime and the limits of physical laws. With the discovery of phenomena such as gravitational lensing [19–21] black hole shadows [6–9], Hawking radiation [10,11], and quasi-normal modes (QNMs) [12–17], the study of black holes has advanced significantly. Recent discoveries, including the first-ever image of a black hole shadow captured by the Event Horizon Telescope collaboration [6–9] and the detection of gravitational waves by [18], have provided new avenues for investigating black hole properties.

Symmetry plays a fundamental role in theoretical physics, with Lorentz symmetry lying at the foundation of both the Standard Model and general relativity (GR). However, it may break at higher energy scales, as suggested by cosmic ray evidence [1–3] and unified gauge theories [5]. Signals of Lorentz violation at lower energies offers experimental opportunities [5]. Theories like loop quantum gravity and the Standard Model Extension (SME) [1–3]. accommodate Lorentz symmetry breaking. In particular, Einstein-bumblebee gravity [4] introduces spontaneous Lorentz symmetry breaking via a bumblebee vector field. Black hole solutions in bumblebee gravity [22] have led to insights into phenomena such as Hawking radiation [23] and traversable wormholes [24]. Within the recent few years, several studies have been made to study the effect of Lorentz violation of different physical systems and contracting the Lorentz violation parameter from different compatible observations [25–32]. bumblebee gravity introduces modifications to spacetime that manifest in various astrophysical observables, such as gravitational lensing, black hole shadows, Hawking radiation, QNMs, and quasi-periodic oscillations (QPOs) [33–50]. The metric-affine bumblebee gravity framework, which treats the metric and affine connections independently has provided new insights [51,52]. It is also, an important model to study the effect of Lorentz violation. Recent studies [53–58] have addressed Lorentz symmetry-breaking (LSB) research significantly, offering new solutions and exploring the effect of the LSB on light deflection and perihelion advance of Mercury. In [59] effects of Lorentz violation on quadrinomial modes have been studied and an attempt has been made to constrain Lorentz violation parameter from the observation of $M87^*$ supermassive black hole.

Hawking radiation, a quantum mechanical effect expected from black holes, depends crucially on the structure of spacetime near the event horizon. The Lorentz-violating parameter modifies the horizon geometry, altering the radiation spectrum and Hawking temperature. Bumblebee gravity, in particular, leads to deviations from the thermal radiation profile predicted by GR. These deviations may be detectable in future observations of black hole thermodynamics, offering a novel way to test and constrain Lorentz-violating effects [23].

QNMs [12–17,60–63] describe the response to the characteristic ringdown frequencies of black holes to perturbations. Since these oscillations are closely tied to the curvature and geometry of the surrounding spacetime, the bumblebee parameter introduces shifts in both the real and imaginary parts of the QNM spectrum [15–17,60,61,63]. These modifications are highly sensitive to the background metric and offer a direct means of testing deviations from classical GR. Gravitational wave observations from LIGO scientific, VRIGO collaboration provide a promising ground for exploring Lorentz violation in strong-field regimes.

One of the most direct effects of Lorentz violation in bumblebee gravity can be observed through the deflection of light around compact objects, influencing gravitational lensing [19–21] and black hole shadows [6–9]. Modifications to the spacetime geometry caused by the Lorentz-violating parameters distort photon trajectories, potentially leading to observable deviations in the size and shape of the black hole's shadow. These distortions are especially relevant in light of precise observations from the Event Horizon Telescope, which captured the shadows of supermassive black holes like $M87^*$ and $Sgr\,A^*$ [6–9]. Comparing these observations with bumblebee gravity predictions allow for potential constraints on the Lorentz violation parameter.

Finally, a promising observational window for constraining the bumblebee parameter lies in the study of [33,34,36–46], which are oscillatory features in the X-ray power spectra of black holes and neutron star systems. These oscillations are tied to the motion of matter in the accretion disk and are influenced by the underlying spacetime geometry. In bumblebee gravity, QPO frequencies are modified due to the altered metric structure introduced by the Lorentz-violating vector field. By comparing observed QPO frequencies with theoretical predictions in the context of bumblebee gravity, stringent constraints on the Lorentz-violating parameter can be established [33,34,36–46].

The effects of Lorentz violation in bumblebee gravity extend beyond classical tests of general relativity, potentially reflecting deeper quantum gravitational phenomena. This interplay between observable astrophysical phenomena and the underlying quantum structure of spacetime provides a promising avenue for constraining the bumblebee parameter. Observational data from black hole shadows, QNMs, and QPOs enhance our ability to probe Lorentz symmetry-breaking effects and test quantum gravity theories [53–57,59].

Thus, the Lorentz violation parameter in metric-affine bumblebee gravity is expected to induce modifications across a range of black hole and strong-field phenomena, including gravitational lensing [19–21], shadows [6–9], thermodynamics [10,11,23], QNMs [12–17,60–63] and QPOs [33,34,36–46]. Among these, QPOs stand out as a particularly effective tool for constraining the bumblebee parameter associated

with metric-affine bumblebee gravity due to their sensitivity to spacetime structure. This interdisciplinary approach, combining astrophysical observations with theoretical predictions, provides a robust framework for testing Lorentz-violating theories and their implications for quantum gravity.

The rest of the paper is organized as follows. In Sect. 2 we have given a brief description of the metric-affine traceless bumblebee mode. Section 3 is devoted to the estimation of Lorentz violating parameter, which has been carried out using observable from shadow $M87^*$ supermassive black hole. In Sect. 4 contains two subsections. In Sect. 4.1 we describe the motion of the particle in a time-like geodesics and compute the epicyclic frequencies analytically. Section 4.2 an attempt has been made to constrain the Lorentz violating parameter by utilizing the observational results of QPOs for microquasars.

2 Description of the metric-affine traceless bumblebee mode

The metric-affine (Palatini) formalism is a prevalent framework in the study of modified gravity theories. Unlike the traditional metric approach, this formalism treats the metric and the affine connection as independent dynamical variables, allowing for greater generality in exploring the structure of spacetime. In their work [56], the authors investigate the traceless metric-affine bumblebee model, which incorporates spontaneous Lorentz symmetry breaking. They derive a static, spherically symmetric vacuum solution under this framework. The action for this model is presented in [56].

$$\mathcal{S}_B = \int d^4x\,\sqrt{-g}\Bigg[\frac{1}{2\kappa^2}\,(\mathcal{R}(\Gamma) +\xi\left(\mathcal{B}^\mu\mathcal{B}^\nu-\frac{1}{4}\mathcal{B}^2 g^{\mu\nu}\right)\mathcal{R}_{\mu\nu}(\Gamma)\Big)-\frac{1}{4}\mathcal{B}^{\mu\nu}\mathcal{B}_{\mu\nu}- - V(\mathcal{B}^\mu\mathcal{B}_\mu\pm b^2)\Bigg]+\int d^4x\sqrt{-g}\mathcal{L}_{mat}(g_{\mu\nu},\psi), \quad (1)$$

where $\mathcal{B}_\mu$ is the bumblebee field, $g^{\mu\nu}$ is traceless metric, and $V(\mathcal{B}^\mu\mathcal{B}_\mu \pm b^2)$ is the potential that spontaneously breaks the Lorentz symmetry when $b^2 = b_\mu b^\mu$ is a real positive constant. The potential is assumed to have a minimum at $V'(b_{mu}b^{mu}) = 0$ and $\mathcal{B}^\mu\mathcal{B}_\mu \pm b^2 = 0$ ensuring the breaking of $U(1)$ symmetry. In this scenario, the bumblebee field acquires a nonzero vacuum expectation value $\langle\mathcal{B}_\mu\rangle = b_\mu$ Additionally, it is assumed that the potential reaches zero at its minimum. The same algebraic manipulation and the assumptions mentioned above served the foundation to derive a static, spherically symmetric metric [56]

$$ds^2 = -\frac{\left(1-\frac{2M}{r}\right)}{\sqrt{\left(1+\frac{3\alpha}{4}\right)\left(1-\frac{\alpha}{4}\right)}}dt^2 +\frac{dr^2}{\left(1-\frac{2M}{r}\right)}\sqrt{\frac{\left(1+\frac{3\alpha}{4}\right)}{\left(1-\frac{\alpha}{4}\right)^3}}+r^2\left(d\theta^2+\sin^2\theta d\phi^2\right), \quad (2)$$

where α is the Lorentz-violating parameter. In the limit $\alpha \to 0$, the Lorentz symmetry breaking (LSB) metric (2) reduces to the Schwarzschild metric. Additionally, there is a noticeable difference between the line elements associated with the bumblebee and metric-affine bumblebee gravity. In the former one, the coefficient of the spacial part only modifies however in the metric-affine bumblebee both spatial and temporal part are modified with different factors containing the Lorentz violation parameter. The Kretschmann scalar invariant corresponding to this metric reads

$$\begin{aligned}\mathcal{K} &= \mathcal{R}_{\lambda\eta\mu\nu}\mathcal{R}^{\lambda\eta\mu\nu}\\ &= \frac{1}{r^6(4+3\alpha)^{3/2}}[48\alpha Mr\sqrt{4+3\alpha}+32M\alpha r\sqrt{4-\alpha}\\ &\quad -12M\alpha^2 r\sqrt{4-\alpha}+32r^2\sqrt{4+3\alpha}+192M^2\sqrt{4+3\alpha}\\ &\quad -32r^2\sqrt{4-\alpha}-16r^2\alpha\sqrt{4-\alpha}-12\alpha^2 Mr\sqrt{4+3\alpha}\\ &\quad +6r^2\alpha^2\sqrt{4-\alpha}+64Mr\sqrt{4-\alpha}-144\alpha M^2\sqrt{4+3\alpha}\\ &\quad -3M^2\alpha^3\sqrt{4+3\alpha}+36M^2\alpha^2\sqrt{4+3\alpha}+3\alpha^2r^2\sqrt{4+3\alpha}\\ &\quad +\alpha^3 Mr\sqrt{4+3\alpha}-64Mr\sqrt{4+3\alpha}-\frac{1}{4}\alpha^3r^2\sqrt{4+3\alpha}].\end{aligned} \quad (3)$$

The expression for the Kretschmann scalar invariant (3) demonstrates that the effects of Lorentz symmetry breaking, as represented by the parameter α, cannot be entirely absorbed for by mere re-scaling of the coordinates. When $\alpha \to 0$ we obtain the anticipated standard result corresponds to the Schwarzschild metric $\mathcal{K}_S = \frac{48M^2}{r^6}$.

3 Parameter estimation using observable from shadow

Validating theoretical models against observational or experimental data requires constraining a free parameter. The precise bounds on the parameter help ensure the physical viability and alignment with known phenomena. In this context, estimating the range of Lorentz violation parameter α parameter is important and useful. One can evaluate the consistency of models such as metric affine bumblebee gravity with data, such as QPOs, lensing, or QMNs, by, for instance, restricting the Lorentz violation parameter to a lower limit. By eliminating or endorsing particular parameter ranges, this procedure improves the prediction ability of a theory. Here we will be using constraints reported in [64–68] obtained from the experimental observation of shadows of supermassive BHs $M87^*$ and $SgrA^*$ consistent with

To this end, we first write the Lagrangian for the metric under consideration:

$$\mathscr{L} = \frac{1}{2}\left(g_{tt}\dot{t}^2 + g_{rr}\dot{r}^2 + g_{\phi\phi}\dot{\phi}^2\right) = \frac{1}{2}\left(-f(r)\dot{t}^2 + \frac{\dot{r}^2}{g(r)} + h(r)\dot{\phi}^2\right), \tag{4}$$

where

$$f(r) = \frac{\left(1-\frac{2M}{r}\right)}{\sqrt{\left(1+\frac{3\alpha}{4}\right)\left(1-\frac{\alpha}{4}\right)}},$$
$$\frac{1}{g(r)} = \frac{1}{\left(1-\frac{2M}{r}\right)}\sqrt{\frac{\left(1+\frac{3\alpha}{4}\right)}{\left(1-\frac{\alpha}{4}\right)^3}}. \tag{5}$$

Here, we have considered that the motion is confined in the equatorial plane $\theta = \pi/2$. Owing to the static and spherically symmetric nature of spacetime, the Lagrangian is independent of time and azimuthal angle. This leads to two conserved quantities of motion. These are as follows:

$$\mathcal{E} = -p_t = -\frac{\partial\mathscr{L}}{\partial\dot{t}} = f(r)\dot{t},$$
$$\mathcal{L} = p_\phi = \frac{\partial\mathscr{L}}{\partial\dot{\phi}} = h(r)\dot{\phi}. \tag{6}$$

Here, $\mathcal{E}$ is the energy and $\mathcal{L}$ is the angular momentum. Four-velocity of a mass-less particle follow the relation $u_\mu u^\mu = 0$ where $u^\mu = \frac{dx^\mu}{d\tau}$. This in combination with Eq. (4) and Eq. (6) leads to the following radial equations:

$$\dot{r}^2 + \left(-\mathcal{E}^2\frac{g(r)}{f(r)} + \mathcal{L}^2\frac{g(r)}{h(r)}\right) = 0$$
$$\Rightarrow \dot{r}^2 + V_{eff}(r) = 0, \tag{7}$$

where $V_{eff} = -\mathcal{E}^2\frac{g(r)}{f(r)} + \mathcal{L}^2\frac{g(r)}{h(r)}$ is the effective potential. Imposing conditions

$$V_{eff}(r_p) = 0, \quad \frac{\partial V_{eff}}{\partial r}|_{r=r_p} = 0, \text{ and } \frac{\partial^2 V_{eff}}{\partial r^2}|_{r=r_p} < 0, \tag{8}$$

on the effective potential we obtain radius r_p of the unstable spherical orbits leading to the relation $f(r)'h(r) = h(r)'f(r)$ whose solution yields r_p. An interesting observation one can make is the non-appearance of $g(r)$ in the relation. One may therefore conclude that if a solution of a proposed model does not affect $f(r)$ or $h(r)$ (e.g. [69]), then the photon orbit has a radius equal to $3M$ which is the case for Schwarzschild BH. In our case, the radius of the photon orbit also comes out to be $3M$. The impact parameter corresponding to the photon orbit is called critical impact parameter b_p as photons with impact parameter $b < b_p$ get swallowed by the BH and those with $b > b_p$ get deflected from their path but can reach the asymptotic observer. However, photons with $b = b_p$ circle around BH several times before either getting swallowed by BH or reaching the observer. The critical impact parameter provides the radius of shadow R_s as [47]

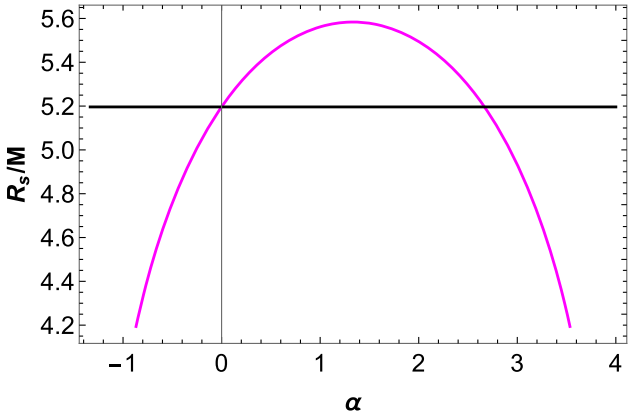

Fig. 1 Variation of R_s against α. The horizontal black line corresponds to $R_s = 3\sqrt{3}M$. Here $M = 1$

$$b_p = R_s = \frac{\mathcal{L}}{\mathcal{E}} = \sqrt{\frac{hr_p}{f(r_p)}} = \frac{3}{2}\sqrt{3}\sqrt[4]{-3\alpha^2+8\alpha+16}M. \tag{9}$$

For $\alpha = 0$, we restore the value for Schwarzschild BH $R_s = 3\sqrt{3}M$. We display graphically qualitative dependence of the radius of the shadow on the parameter α in Fig. 1. It reveals that initially, the radius of the shadow increases with α, reaching a maximum value $5.58363M$ at $\alpha = \frac{4}{3}$ and then starts decreasing. Another interesting observation one can make from the figure is that apart from $\alpha = 0$, we have $R_s = 3\sqrt{3}M$ for $\alpha = \frac{8}{3}$.

To employ observations regarding shadows of $M87^*$ and $SgrA^*$ for constraining α, we introduce the parameter δ defined by [70]

$$\delta = \frac{R_s}{3\sqrt{3}M} - 1 = \frac{1}{2}\sqrt[4]{-3\alpha^2+8\alpha+16} - 1. \tag{10}$$

It is the deviation of the shadow radius from the Schwarzschild case.

Similar to the case of the radius of the shadow the deviation parameter too initially increases with α reaching a maximum value 0.0745699 at $\alpha = \frac{4}{3}$ and then starts decreasing, as evident from Fig. 2. Bounds on the deviation parameter are given below [64–68] (Table 1).

Subjecting our theoretical prediction to the above bounds, we obtain the following ranges for the parameter α that make our model consistent with the experimental observations.

In addition to bounds on the deviation parameter, we will also use angular diameter data related to constraining α. The angular diameter is defined as

$$\theta_d = \frac{2R_s}{D}, \tag{11}$$

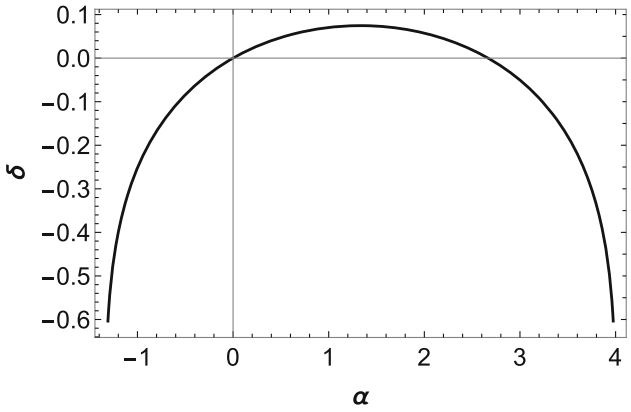

Fig. 2 Variation of δ against α

where D is the distance of the BH from Earth. According to EHT collaboration [6,71,72], mass, distance, and angular diameter of $M87^*$ BH are $M = 6.5 \pm 0.7 \times 10^9 M_\odot$, $D = 16.8 \pm 0.8$ Mpc, and $\theta_d = 42 \pm 3$ μas, respectively. Those values for $SgrA^*$ are $M = 4.3 \pm 0.013 \times 10^6 M_\odot$, $D = 8.277 \pm 0.033$ kpc, and $\theta_d = 48.7 \pm 7$ μas [8,67,68]. We use $M = 6.5 \times 10^9 M_\odot$, $D = 16.8$ Mpc for $M87^*$ and $M = 4.3 \times 10^6 M_\odot$, $D = 8.277$ kpc for $SgrA^*$. We illustrate the variation of angular diameter calculated using Eq. (11) with α in Fig. 3.

We can observe from the above figure that even though the angular diameter for $SgrA^*$ touches the upper bound in 1σ confidence level, i.e. 55.7 μas, it never happens for the $M87^*$ BH. Matching the theoretical prediction and experimental observations, we obtain $\alpha \in [-0.106801, 2.77347]$ within 1σ confidence level and $\alpha \in [-0.52517, 3.19184]$ within 2σ confidence level for $M87^*$, whereas, for $SgrA^*$ $\alpha \in [-0.921827, 0.5186] \cup [2.14807, 3.58849]$ within 1σ confidence level and $\alpha \in [-1.14457, 3.81123]$ within 2σ confidence level. Our analysis in this section provides a range of values of the parameter α that make the model under consideration concordant with observed bounds on various observables related to the shadow of BHs $M87^*$ and $SgrA^*$. In the following section we will be using observed QPOs of microquasars to constrain the parameter α.

4 Estimation of the LSB parameter using observational results of QPOs for microquasars

Before delving into details of QPO, needs to calculate conserved quantities for a test particle in a time-like geodesics and to obtain effective potential, specific energy, and angular momentum for a test particle in an equatorial circular orbit. These quantities are essential in the study of the epicyclic motion.

4.1 Motion of the particle in a time-like geodesics

The Lagrangian for a test particle is given in Eq. (4) and its conserved quantities are given in Eq. (6). However, in the case of time-like geodesics, $\mathcal{E}$ and $\mathcal{L}$ are specific energy and specific angular momentum, respectively. The four-velocity of the test particle follows the relation $u_\mu u^\mu = -1$ that provides the radial equation of motion in the equatorial plane as

$$g_{rr}\dot{r}^2 = -\frac{1}{g_{tt}}\left[\mathcal{E}^2 + g_{tt}\left(1 + \frac{\mathcal{L}^2}{g_{\phi\phi}}\right)\right] = -\frac{1}{g_{tt}}\left[\mathcal{E}^2 - \mathcal{V}_{\text{eff}}\right].$$

Here, $\mathcal{V}_{\text{eff}} = -g_{tt}(1 + \frac{\mathcal{L}^2}{g_{\phi\phi}})$ is the effective potential. For motion in a circular orbit of radius r_0, we have

$$\mathcal{V}_{\text{eff}}(r_0) = \mathcal{E}^2, \quad \frac{\partial \mathcal{V}_{\text{eff}}}{\partial r}|_{r=r_0} = 0. \tag{12}$$

Table 1 Bounds on δ from different observatories

BH	Observatory	δ	1σ bounds	2σ bounds
$M87^*$	EHT	$-0.01^{+0.17}_{-0.17}$	$4.26 \leq \frac{R_s}{M} \leq 6.03$	$3.38 \leq \frac{R_s}{M} \leq 6.91$
$SgrA^*$	VLTI	$-0.08^{+0.09}_{-0.09}$	$4.31 \leq \frac{R_s}{M} \leq 5.25$	$3.85 \leq \frac{R_s}{M} \leq 5.72$
	Keck	$-0.04^{+0.09}_{-0.10}$	$4.47 \leq \frac{R_s}{M} \leq 5.46$	$3.95 \leq \frac{R_s}{M} \leq 5.92$

Table 2 Bounds on α from different observatories

BH	Observatory	δ	1σ bounds	2σ bounds
$M87^*$	EHT	$-0.01^{+0.17}_{-0.17}$	$[-0.834568, 3.50123]$	$[-1.14842, 3.81508]$
$SgrA^*$	VLTI	$-0.08^{+0.09}_{-0.09}$	$[-0.80676, 0.0838442] \cup [2.58282, 3.47343]$	$[-1.01439, 3.68106]$
	Keck	$-0.04^{+0.09}_{-0.10}$	$[-0.714528, 0.540609] \cup [2.12606, 3.38119]$	$[-0.975735, 3.6424]$

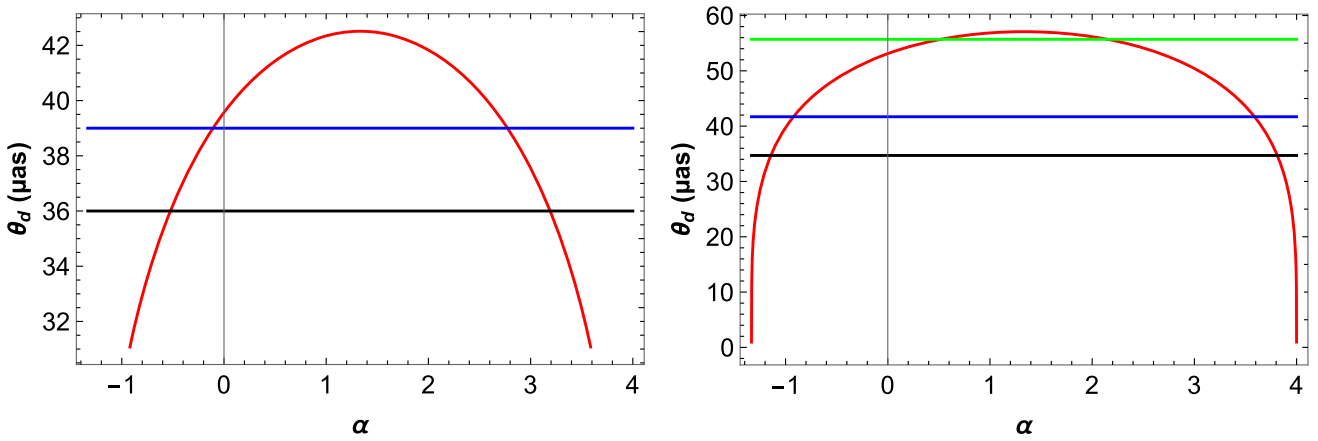

Fig. 3 Variation of angular diameter with α. The left panel is for $M87^*$ where blue and black horizontal lines correspond to $\theta_d = 39$ μas and 36 μas. The right panel is for $Sgr\,A^*$ where green, blue, and black horizontal lines are for 55.7 μas, 41.7 μas, and 34.7 μas, respectively

The second condition provides the expression for $\mathcal{L}$ and then we obtain $\mathcal{E}$ using the first condition as

$$\mathcal{L}^2 = \frac{-g'_{tt}g^2_{\phi\phi}}{g_{\phi\phi}g'_{tt} - g_{tt}g'_{\phi\phi}}, \quad \mathcal{E}^2 = \frac{g^2_{tt}g'_{\phi\phi}}{g_{\phi\phi}g'_{tt} - g_{tt}g'_{\phi\phi}}, \tag{13}$$

where $'$ represents differentiation with respect to r. For stable circular orbit, we must have $\frac{\partial^2\mathcal{V}_{\rm eff}}{\partial r^2}|_{r=r_0} > 0$. The limiting case is the innermost circular orbit(ISCO) where we have $\frac{\partial^2\mathcal{V}_{\rm eff}}{\partial r^2}|_{r=r_0} = 0$ which comes out to $6M$ for the metric-affine metric. Thus, similar to the event horizon an photon orbit, the ISCO radius too does not depend on α and matches with that for a Schwarzschild BH. The effective potential $\mathcal{V}_{\rm eff}$ and the conserved quantities provide the prerequisite platform to study QPOs of microquasars.

4.2 Epicyclic frequencies

When a test particle is perturbed from its stable circular orbit of radius r_0 in the equatorial plane, it undergoes epicyclic oscillations, known as quasi-periodic oscillations. The epicyclic motion has two components: radial component in the equatorial plane and latitudinal component normal to the equatorial plane. If the equatorial circular orbit is perturbed by $r = r_0 + \delta r$ in the radial direction and $\theta = \frac{\pi}{2} + \delta\theta$ in the latitudinal direction, where δr and $\delta\theta$ are small quantities, then the differential equations of motion governing radial and latitudinal oscillations are

$$\delta\ddot{r} + \Omega_r^2\delta r = 0, \quad \delta\ddot{\theta} + \Omega_\theta^2\delta\theta = 0, \tag{14}$$

where Ω_r and Ω_θ are locally defined radial and latitudinal angular frequencies and the dot represents differentiation with respect to the proper time. To obtain these epicyclic frequencies, we first separate Hamiltonian into dynamical $\mathcal{H}_{dyn}$ and $\mathcal{H}_{pot}$ parts where

$$\mathcal{H}_{dyn} = \frac{1}{2}\left(\frac{p_r^2}{g_{rr}} + \frac{p_\theta^2}{g_{\theta\theta}}\right),$$
$$\mathcal{H}_{pot} = \frac{1}{2}\left(\frac{\mathcal{E}^2}{g_{tt}} + \frac{\mathcal{L}^2}{g_{\phi\phi}} + 1\right). \tag{15}$$

It is the potential part of the Hamiltonian that governs the local epicyclic oscillations. The epicyclic frequencies Ω_r and Ω_θ along with Ω_ϕ are given by [73,74]

$$\Omega_r^2 = \frac{1}{g_{rr}}\frac{\partial^2\mathcal{H}_{pot}}{\partial r^2},$$
$$\Omega_\theta^2 = \frac{1}{g_{rr}}\frac{\partial^2\mathcal{H}_{pot}}{\partial\theta^2},$$
$$\Omega_\phi^2 = \frac{\mathcal{L}}{g_{\phi\phi}}. \tag{16}$$

We must now transform these locally defined angular frequencies to those measured at spatial infinity. This is done by taking into consideration the redshift factor. Hence, the required transformation from the locally measured angular frequencies Ω to those measured at spatial infinity ω is [73,74]

$$\omega \to \frac{\Omega}{-g^{tt}\mathcal{E}}. \tag{17}$$

Utilizing expressions for conserved quantities given in Eq. (13) along with Eqs. (16) and (17), we obtain the following expressions for radial and latitudinal frequencies in terms of metric coefficients:

$$\nu_r = \frac{1}{2\pi}\sqrt{\frac{2g_{\phi\phi}g'^2_{tt} - 2g_{tt}g'_{tt}g_{\phi\phi} - g_{tt}g_{\phi\phi}g''_{tt}}{2g_{tt}g_{rr}g_{\phi\phi}} + \frac{g'_{tt}g''_{\phi\phi}}{2g_{rr}g'_{\phi\phi}}}, \tag{18}$$

$$\nu_\theta = \nu_\phi = \frac{1}{2\pi}\sqrt{-\frac{g'_{tt}}{g'_{\phi\phi}}}. \tag{19}$$

For the metric under consideration, we have

$$\begin{aligned} g_{tt} &= -c^2\frac{1-\frac{2GM}{c^2 r}}{\sqrt{\left(1-\frac{\alpha}{4}\right)\left(\frac{3\alpha}{4}+1\right)}},\\ g_{rr} &= \frac{\sqrt{\frac{\frac{3\alpha}{4}+1}{\left(1-\frac{\alpha}{4}\right)^3}}}{1-\frac{2GM}{c^2 r}},\\ g_{\phi\phi} &= r^2. \end{aligned} \tag{20}$$

Putting the above metric coefficients in Eq. (19) yields

$$\begin{aligned} \nu_r &= \frac{1}{2\pi}\frac{c^3}{GM}\sqrt{\frac{(\alpha-4)(2-y)}{(3\alpha+4)y^4}},\\ \nu_\theta = \nu_\phi &= \frac{1}{2\pi}\frac{c^3}{GM}\sqrt{\frac{4}{\sqrt{-3\alpha^2+8\alpha+16}y^3}}, \end{aligned} \tag{21}$$

where $y = r/r_g$, $r_g = \frac{GM}{c^2}$, G and c being gravitational constant and speed of light, respectively.

4.3 Constraining the LSB parameter from QPOs of microquasars

Apart from the estimation of the LSB parameter from the observation of shadow of black hole we can exploit observed high-frequency QPOs (HFQPOs) of microquasars in order to constrain LSB parameter α. Now we are in a position to proceed to wads that endeavor. The process of constraining the parameter α by utilizing observed high-frequency QPOs (HFQPOs) of microquasars is indeed instructive and noteworthy. The theoretical studies suggest that the magnitude of QPOs has a precise dependence on the mass of the BH. From recent observations, it is found that the HFQPOs are often observed in the rational ratio [75], especially in the ratio 3:2 [76], Two such microquasars which show twin peaks in their power spectrum in the ratio $3:2$ are $GROJ1655-40$ and $XTEJ1550-564$ galactic microquasars. Their lower (ν_L) and upper (ν_U) QPOs along with their observed masses are as follows [77–79]:

$$\begin{aligned} &\text{GRO J1655-40:}\frac{M}{M_\odot} = 6.30 \pm 0.27,\\ &\nu_U = 450 \pm 3\ \text{Hz}, \quad \nu_L = 300 \pm 5\ \text{Hz}, \end{aligned} \tag{22}$$

$$\begin{aligned} &\text{XTE J1550-564:}\frac{M}{M_\odot} = 9.10 \pm 0.60,\\ &\nu_U = 276 \pm 3\ \text{Hz}, \quad \nu_L = 184 \pm 5\ \text{Hz}. \end{aligned} \tag{23}$$

Resonance between radial and vertical oscillations of infilling particles, especially near ISCO radius, is considered to be one of the viable explanations for the appearance of twin peaks. This model, known as resonance model, considers non-linear coupling between the two oscillations responsible for QPOs [80,81]. The frequency ratio ν_U/ν_L for HFQPOs points towards resonance phenomenon. We will consider the forced resonance model [82] where

$$\nu_L = \nu_\theta \quad \text{and} \quad \nu_U = \nu_r + \nu_\theta. \tag{24}$$

We are going to employ the above model in order to bound α. In Figs. 4 and 5, we fit upper and lower frequencies obtained theoretically treating microquasars as LSB BH under consideration to the observed frequencies. Frequency curves do not intersect the mass error bands for both the microquasars when $\alpha = 0.2$ implying incommensuration of our BH model with observed values when $\alpha = 0.2$.

Figures 4 and 5 exhibit the fact that our BH model is not concordant with observed values of QPOs for all values of α. To obtain parameter values that make our model commensurate with the experimental observations, we provide variation of lower frequency ν_L as a function of mass and LSB parameter in Fig. 6.

The region between two solid lines provides the parameter space where observed values match theoretical predictions. We obtain the following sets of values of α from observations:

$$\begin{aligned} &\text{For GRO J1655-40:} \quad \alpha \in [0.422039, 0.471269],\\ &\text{For XTE J1550-564:} \quad \alpha \in [0.459285, 0.528621]. \end{aligned} \tag{25}$$

Interestingly, the above ranges of values do not include $\alpha = 0$ thereby ruling out Schwarzschild BH as a viable candidate that may exhibit observed QPO peaks in its power spectrum. Our analysis in this section makes the claim that our considered model is a feasible candidate that generates astrophysical observations commensurate with experimental results stronger.

5 Concluding remarks

In this manuscript, we study imprints of LSB, emanating in the metric-affine bumblebee model, from the observed shadows of $M87^*$ and $SgrA^*$ BHs and the observed QPOs of GRO J1655-40 and XTE J1550-564 galactic microquasars. These BHs (traceless metric-affine BHs) provide an excellent opportunity to probe one of the fundamental pillars of physics, the Lorentz symmetry. Astrophysical observations such as shadow and QPOs have little dependence on the complex physics related to accretion. As such, they provide a potent and cleaner tool to probe the nature of the underlying spacetime. Here we intend to find out the signature of LSB from observables related to shadow and QPOs.

We first investigated the impact of LSB on the radius of the unstable photon orbit and the corresponding critical impact parameter. We have found the radius of the photon orbit independent of the LSB parameter. Its value came out

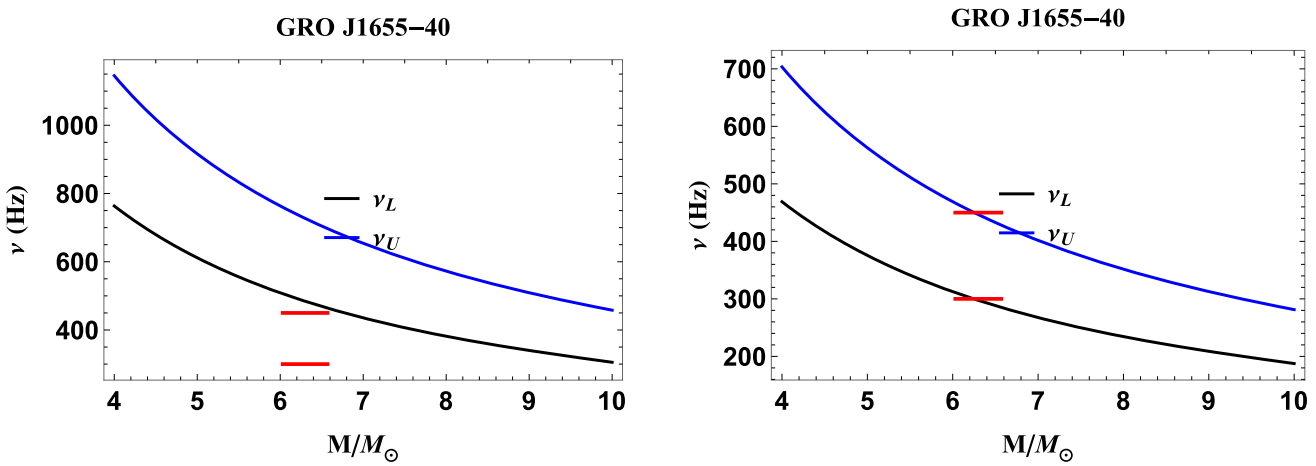

Fig. 4 Fitting the upper and lower frequencies to the observed frequencies for the GRO J1655-40 microquasar The left one is for $\alpha = 0.2$ and the right one is for $\alpha = 0.45$. Horizontal lines show the mass error band for GRO J1655-40

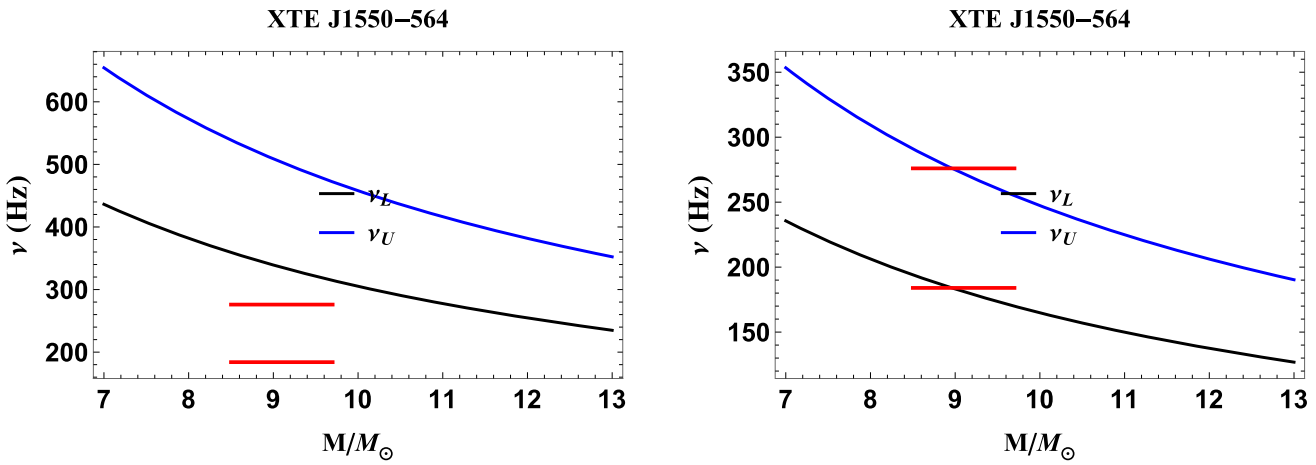

Fig. 5 Fitting the upper and lower frequencies to the observed frequencies for the XTE J1550-564 microquasar The left one is for $\alpha = 0.2$ and the right one is for $\alpha = 0.5$. Horizontal lines show the mass error band for XTE J1550-564

to be $3M$ which is the value for a Schwarzschild BH. However, the critical impact parameter corresponding to the photon orbit (shadow radius) has a significant dependence on α. The shadow radius initially increases with α, reaching a maximum value of $5.58363M$ at $\alpha = \frac{4}{3}$, and then starts decreasing. Interestingly, in addition to $\alpha = 0$, the shadow radius for the BH under consideration is equal to that for a Schwarzschild BH for $\alpha = \frac{8}{3}$ as well. Introducing the deviation parameter δ, we then utilize its observed bounds for $M87^*$ and $SgrA^*$ BHs reported by EHT, Keck, and VLTI to gauge the viability of our BH model. We have tabulated obtained bounds on α in Table 2. We have also employed bounds on their angular diameters to constrain parameter values of α. Our analysis in this regard has exhibited commensurability of our model with observed results for a wide range of values of α.

The motion of test particles in the background of a BH embeds information regarding background spacetime. We have obtained the effective potential for a test particle confined in an equatorial circular orbit. The ISCO radius is obtained by equating the double derivative of the effective potential to zero came out to be $6M$, independent of α, and equals that for a Schwarzschild BH. We have stable circular orbits when $\frac{\partial^2 \mathcal{V}_{\text{eff}}}{\partial r^2} > 0$. Thus, stable circular orbits must lie outside ISCO. When a particle in a stable circular orbit lying on a latitudinal plane Θ is perturbed in radial as well as latitudinal directions, it undergoes epicyclic oscillations in two mutually perpendicular directions: one in the radial direction in Θ plane and another in latitudinal direction normal to the Θ plane. In this manuscript, we have considered the perturbation of the equatorial circular orbit. Observed HFQPOs in the power spectrum of galactic microquasars are especially interesting as they mostly occur in the rational ratio, especially in the ratio 3:2 [76]. We have selected two microquasars GRO J1655-40 and XTE J1550-564 with the known QPO data to constrain the LSB parameter. The observed ratio between

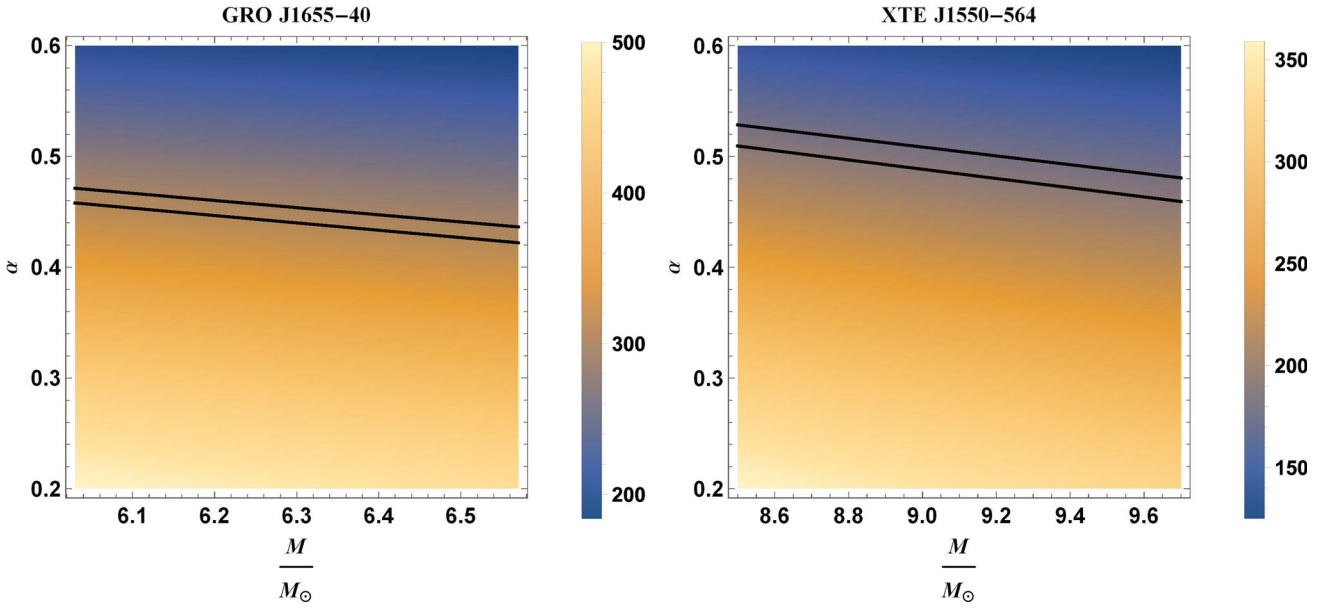

Fig. 6 Variation of lower QPO frequency ν_L with mass of the BH and LSB parameter α. The left one is for GRO J1655-40 and the right one is for XTE J1550-564. In each plot, the upper solid black line corresponds to the upper 1σ bound, and the lower one is for the lower 1σ bound of ν_L

lower and higher QPOs points towards resonance between the two epicyclic oscillations. We have used the forced resonance model. Bound on the parameter α from QPOs are: for GRO J1655-40 $\alpha \in [0.422039, 0.471269]$ and for XTE J1550-564 $\alpha \in [0.459285, 0.528621]$. These bounds are stronger than those found from shadow observables. We may obtain fine bounds on the parameter α with an improved precision. This we may achieve in the future with European Space Agency (ESA) X-ray mission LOFT.

Regarding our observation of the constraints on α it would be beneficial to make a comparison of the constraints obtained recently from different experimental data. We find α falls within the range $\alpha \in [-0.106801, 2.77347]$ at the 1σ confidence level and $\alpha \in [-0.52517, 3.19184]$ at the 2σ confidence level for $M87^*$. For $SgrA^*$, we find that $\alpha \in [-0.921827, 0.5186] \cup [2.14807, 3.58849]$ within the 1σ confidence level, while within the 2σ confidence level, α extends to $\alpha \in [-1.14457, 3.81123]$.

In [47], the authors showed that for Sgr A^*, the observational data suggests α lies in the range $0 < \alpha < 0.037$ at the 1σ confidence level, which extends to $0 < \alpha < 0.86$ at the 2σ confidence level. Notably, both of these ranges fall within the limits we have reported here.

Furthermore, from the quasi-periodic oscillation (QPO) frequency data, we observed that for GRO J1655-40: $\alpha \in [0.422039, 0.471269]$, and for XTE J1550-564: $\alpha \in [0.459285, 0.528621]$. These constraints on α are in agreement with our findings concerning the shadow radius data. Additionally, [49] revealed that the upper bound on α derived from observational data of perihelion of Mercury precession was $\alpha < 7.4 \times 10^{-12}$, which is in agreement with the findings of the papers [22,83,84].

Acknowledgements

Funding No fund was provided from any sources. We did this work in our own interest.

Data Availability Statement This manuscript has no associated data. [Author's' comment: Data sharing not applicable to this article as no datasets were generated or analysed during the current study.]

Code Availability Statement This manuscript has no associated code/software. [Author's comment: Code/Software sharing not applicable to this article as no code/software was generated or analysed during the current study.]

Open Access This article is licensed under a Creative Commons Attribution 4.0 International License, which permits use, sharing, adaptation, distribution and reproduction in any medium or format, as long as you give appropriate credit to the original author(s) and the source, provide a link to the Creative Commons licence, and indicate if changes were made. The images or other third party material in this article are included in the article's Creative Commons licence, unless indicated otherwise in a credit line to the material. If material is not included in the article's Creative Commons licence and your intended use is not permitted by statutory regulation or exceeds the permitted use, you will need to obtain permission directly from the copyright holder. To view a copy of this licence, visit http://creativecommons.org/licenses/by/4.0/.
Funded by SCOAP[3].

References

1. V.A. Kostelecky, R. Potting, CPT, strings, and meson factories. Phys. Rev. D **51**, 3923 (1995)

2. D. Colladay, V.A. Kostelecky, CPT violation and the standard model. Phys. Rev. D **55**, 6760 (1997)
3. V.A. Kostelecky, S. Samuel, Spontaneous breaking of Lorentz symmetry in string theory. Phys. Rev. D **39**, 683 (1989)
4. V.A. Kostelecky, Gravity, Lorentz violation, and the standard model. Phys. Rev. D **69**, 105009 (2004). arXiv:hep-th/0312310
5. V.A. Kostelecky, S. Samuel, Photon and graviton masses in string theories. Phys. Rev. Lett. **66**, 1811 (1991)
6. K. Akiyama et al., First M87 Event Horizon Telescope results. I. The shadow of the supermassive black hole. Astrophys. J. Lett. **875**, L1 (2019)
7. K. Akiyama et al., First M87 Event Horizon Telescope results. IV. Imaging the central supermassive black hole. Astrophys. J. Lett. **875**(1), L4 (2019)
8. K. Akiyama et al., First Sagittarius A* Event Horizon Telescope results. I. The shadow of the supermassive black hole in the center of the Milky Way. Astrophys. J. Lett. **930**(2), L12 (2022)
9. K. Akiyama et al., First Sagittarius A* Event Horizon Telescope results. II. EHT and multiwavelength observations, data processing, and calibration. Astrophys. J. Lett. **930**(2), L13 (2022)
10. S.W. Hawking, Commun. Math. Phys. **43**, 199 (1975). [Erratum: Commun. Math. Phys. **46**, 206 (1976)]
11. J.D. Bekenstein, Phys. Rev. D **7**, 2333 (1973)
12. T. Regge, J.A. Wheeler, Stability of a Schwarzschild singularity. Phys. Rev. **108**, 1063 (1957)
13. H.W. Press, Long wave trains of gravitational waves from a vibrating black hole. Astrophys. J. **170**, L105–L108 (1971)
14. V.C. Vishveshwara, Scattering of gravitational radiation by a Schwarzschild black-hole. Nature **227**, 936–938 (1970)
15. K.D. Kokkotas, B.G. Schmidt, Living Rev. Relativ. **2**, 2 (1999). arXiv:gr-qc/9909058
16. H.-P. Nollert, Class. Quantum Gravity **16**, R159 (1999)
17. H.-P. Nollert, Detection of the Schwarzschild precession in the orbit of the star S2 near the Galactic centre massive black hole. Astron. Astrophys. **636**, L5 (2020)
18. B.P. Abbott et al., GW150914: the advanced LIGO detectors in the era of first discoveries. Phys. Rev. Lett. **116**(13), 131103 (2016)
19. C.W. Misner, K.S. Thorne, J.A. Wheeler, *Gravitation* (W. H. Freeman and Company, New York, 1971)
20. S. Weinberg, *Gravitation and Cosmology* (Wiley, New York, 1972)
21. S. Chandrasekhar, The *Mathematical Theory of Black Holes. Oxford Classic Texts in the Physical Sciences (1983)* Paperback – 3 September 1998
22. R. Casana, A. Cavalcante, F.P. Poulis, E.B. Santos, Exact Schwarzschild-like solution in a bumblebee gravity model. Phys. Rev. D **97**, 104001 (2018)
23. S. Kanzi, I. Sakalli, GUP modified Hawking radiation in bumblebee gravity. Nucl. Phys. B **946**, 114703 (2019). arXiv:1905.00477 [hep-th]
24. A. Ovgun, K. Jusufi, I. Sakall, Exact traversable wormhole solution in bumblebee gravity. Phys. Rev. D **99**, 024042 (2019). arXiv:1804.09911 [gr-qc]
25. R.V. Maluf, C.A.S. Almeida, R. Casana, M. Ferreira, Einstein–Hilbert graviton modes modified by the Lorentz violating bumblebee field. Phys. Rev. D **90**, 025007 (2014). arXiv:1402.3554 [hep-th]
26. J. Paramos, G. Guiomar, Astrophysical constraints on the bumblebee model. Phys. Rev. D **90**, 082002 (2014). arXiv:1409.2022 [astro-ph]
27. C.A. Escobar, A. Martn-Ruiz, Equivalence between bumblebee models and electrodynamics in a nonlinear gauge. Phys. Rev. D **95**, 095006 (2017). arXiv:1703.01171 [hep-th]
28. D. Capelo, J. Paramos, Cosmological implications of bumblebee vector models. Phys. Rev. D **91**, 104007 (2015). arXiv:1501.07685 [gr-qc]
29. W. Liu, X. Fang, J. Jing, J. Wang, Exact Kerr-like solution and its shadow in a gravity model with spontaneous Lorentz symmetry breaking. Eur. Phys. J. C **83**, 83 (2023). arXiv:2211.03156 [gr-qc]
30. J.F. Assunao, T. Mariz, J.R. Nascimento, A.Y. Petrov, Dynamical Lorentz symmetry breaking in a tensor bumblebee model. Phys. Rev. D **100**, 085009 (2019). arXiv:1902.10592 [hep-th]
31. A. Uniyal, S. Kanzi, I. Sakall, Greybody factors of bosons and fermions emitted from higher dimensional dS/AdS black holes in Einstein-bumblebee gravity theory. Eur. Phys. J. C **83**, 668 (2023). arXiv:2207.10122 [hep-th]
32. M. Khodadi, M. Schreck, Hubble tension as a guide for refining the early Universe: cosmologies with explicit local Lorentz and diffeomorphism violation. Phys. Dark Universe **39**, 101170 (2023)
33. L. Stella, M. Vietri, Phys. Rev. Lett. **82**, 17–20 (1999). https://doi.org/10.1103/PhysRevLett.82.17. arXiv:astro-ph/9812124
34. L. Stella, M. Vietri, Astrophys. J. Lett. **492**, L59 (1998). https://doi.org/10.1086/311075. arXiv:astro-ph/9709085
35. C. GermanA, Phys. Rev. D **98**, 083025 (2018). arXiv:1810.12426 [astro-ph.HE]
36. C. Bambi, Phys. Rev. D **85**(45), 043002 (2012). arXiv:1201.1638 [grqc]
37. C. Bambi, J. Jiang, J.F. Steiner, Class. Quantum Gravity **33**, 064001 (2016). arXiv:1511.07587 [gr-qc]
38. A. Tripathi, J. Yan, Y. Yang, Y. Yan, M. Garnham, Y. Yao, S. Li, Z. Ding, A.B. Abdikamalov, D. Ayzenberg, C. Bambi, T. Dauser, J.A. Garcia, J. Jiang, S. Nampalliwar Astrophys. J. **874**:135 (2019). arXiv:1901.03064 [gr-qc]
39. M. Tarnopolski, V. Marchenko, Astrophys. J. **911**, 20 (2021). arXiv:2102.05330 [astro-ph.HE]
40. V.I. Dokuchaev, Y.N. Eroshenko, Phys. Usp. **58**, 772 (2015). arXiv:1512.02943 [astro-ph.HE]
41. M. Kološ, Z. Stuchlík, A. Tursunov, Class. Quantum Gravity **32**, 165009 (2015). arXiv:1506.06799 [gr-qc]
42. A.N. Aliev, G.D. Esmer, P. Talazan, Class. Quantum Gravity **30**, 045010 (2013). arXiv:1205.2838 [gr-qc]
43. Z. Stuchlik, P. Slany, G. Torok, Astron. Astrophys. **470**, 401 (2007). arXiv:0704.1252 [astro-ph]
44. L. Titarchuk, N. Shaposhnikov, Astrophys. J. **626**, 298 (2005). arXiv:astro-ph/0503081
45. J. Rayimbaev, B. Majeed, M. Jamil, K. Jusufi, A. Wang, Phys. Dark Universe **35**, 100930 (2022). arXiv:2202.11509 [gr-qc]
46. M. Ghasemi-Nodehi, M. Azreg-Aïnou, K. Jusufi, M. Jamil, Phys. Rev. D **102**, 104032 (2020). arXiv:2011.02276 [gr-qc]
47. A.A. Araújo Filho, H. Hassanabadi, N. Heidari, J. Kríz, S. Zare, Class. Quantum Gravity **41**, 055003 (2024)
48. X.-J. Gao, Eur. Phys. J. C **84**, 973 (2024)
49. J.R. Nascimento, A.Yu. Petrov, P.J. Porfírio, A.R. Soares, Phys. Rev. D **102**, 044021 (2020)
50. G. Lambiase, R.C. Pantig, A. Övgün, EPL **148**, 49001 (2024)
51. D.M. Ghilencea, Eur. Phys. J. C **80**, 1147 (2020). arXiv:2003.08516 [hep-th]
52. D.M. Ghilencea, Palatini quadratic gravity: spontaneous breaking of gauged scale symmetry and inflation. Eur. Phys. J. C **81**, 518 (2021). arXiv:2007.14733 [hep-th]
53. A. Delhom, J. Nascimento, G.J. Olmo, A.Y. Petrov, P.J. Porfirio, Metric-affine bumblebee gravity: classical aspects. Eur. Phys. J. C **81**, 287 (2021). arXiv:1911.11605 [hep-th]
54. A. Delhom, J. Nascimento, G.J. Olmo, A.Y. Petrov, P. Porfirio, Radiative corrections in metric-affine bumblebee model. Phys. Lett. B **826**, 136932 (2022). arXiv: 2010.06391 [hep-th]
55. A. Delhom, T. Mariz, J.R. Nascimento, G.J. Olmo, A.Y. Petrov, P.J. Porfirio, Spontaneous Lorentz symmetry breaking and one-loop effective action in the metric-affine bumblebee gravity. JCAP **07**, 018 (2022). arXiv:2202.11613 [hep-th]

56. A. A. Araujo Filho, J. R. Nascimento, A. Y. Petrov, P. J. Porfírio, Vacuum solution within a metric-affine bumblebee gravity. Phys. Rev. D **108**, 085010 (2023). arXiv:2211.11821 [gr-qc]
57. G. Lambiase, L. Mastrototaro, R.C. Pantig, A. Ovgun, Probing Schwarzschild-like black holes in metric-affine bumblebee gravity with accretion disk, deflection angle, greybody bounds, and neutrino propagation. JCAP **12**, 026 (2023)
58. A.A. Araujo Filho, J.R. Nascimento, AYu. Petrov, P.J. Porfírio, An exact stationary axisymmetric vacuum solution within a metric-affine bumblebee gravity. JCAP **07**, 004 (2024)
59. S.K. Jha, A. Rahaman, Nucl. Phys. B **1002**, 116536 (2024)
60. R.A. Konoplya, A. Zhidenko, Rev. Mod. Phys. **83**, 793 (2011). arXiv:1102.4014 [gr-qc]
61. E. Berti, V. Cardoso, A.O. Starinets, Class. Quantum Gravity **26**, 163001 (2009). arXiv:0905.2975 [gr-qc]
62. L. Barack et al., Class. Quantum Gravity **36**, 143001 (2019). arXiv:1806.05195 [gr-qc]
63. R. Konoplya, A. Zhidenko, Phys. Lett. B **756**, 350 (2016). arXiv:1602.04738 [gr-qc]. arXiv:2309.13594 [gr-qc]
64. K. Akiyama et al., First Sagittarius A^* Event Horizon Telescope results. VI. Testing the black hole metric. Astrophys. J. Lett. **930**(2), L17 (2022)
65. P. Kocherlakota et al., Constraints on black-hole charges with the 2017 EHT observations of $M87^*$. Phys. Rev. D **103**(10), 104047 (2021)
66. T. Do et al., Relativistic redshift of the star S0–2 orbiting the Galactic center supermassive black hole. Science **365**(6454), 664–668 (2019)
67. R. Abuter et al., Mass distribution in the Galactic Center based on interferometric astrometry of multiple stellar orbits. Astron. Astrophys. **657**, L12 (2022)
68. R. Abuter et al., Polarimetry and astrometry of NIR flares as event horizon scale, dynamical probes for the mass of Sgr A^*. Astron. Astrophys. **677**, L10 (2023)
69. R. Casana, A. Cavalcante, F.P. Poulis, E.B. Santos, An exact Schwarzschild-like solution in a bumblebee gravity model. Phys. Rev. D **97**, 104001 (2018). arXiv:1711.02273 [gr-qc]
70. K. Akiyama et al., First Sagittarius A^* Event Horizon Telescope results. Astrophys. J. Lett. **930**, L12 (2022)
71. K. Akiyama et al., First M87 Event Horizon Telescope results. V. Physical origin of the asymmetric ring. Astrophys. J. Lett. **875**(1), L5 (2019)
72. K. Akiyama et al., First M87 Event Horizon Telescope results. VI. The shadow and mass of the central black hole. Astrophys. J. Lett. **875**(1), L6 (2019)
73. S. Shaymatov, J. Vrba, D. Malafarina, B. Ahmedov, Z. Stuchlík, Phys. Dark Universe **30**, 100648 (2020). arXiv:2005.12410 [gr-qc]
74. Z. Stuchlík, J. Vrba, Eur. Phys. J. Plus **136**, 1127 (2021). arXiv:2110.10569 [gr-qc]
75. J.E. McClintock, R.A. Remillard, *Black Hole Binaries*, vol. 39 (Cambridge University Press, Cambridge, 2006), pp.157–213
76. G. Török, A. Kotrlova, E. Sramkova, Z. Stuchlik, Confronting the models of 3:2 quasiperiodic oscillations with the rapid spin of the microquasar GRS 1915+105. Astronom. Astrophys. **531**, 7 (2011)
77. M.E. Beer, P. Podsiadlowski, The quiescent light curve and evolutionary state of GRO J1655–40. Mon. Not. R. Astron. Soc. **331**, 351 (2002). arXiv:astro-ph/0109136
78. S.E. Motta et al., Precise mass and spin measurements for a stellar-mass black hole through X-ray timing: the case of GRO J1655–40. Mon. Not. R. Astron. Soc. **437**(3), 2554–2565 (2014). arXiv:1309.3652 [astro-ph.HE]
79. J.A. Orosz, J.F. Steiner, J.E. McClintock, M.A.P. Torres, R.A. Remillard, C.D. Bailyn, J.M. Miller, An improved dynamical model for the microquasar XTE J1550–564. Astrophys. J. **730**, 75 (2011). arXiv:1101.2499 [astro-ph.SR]
80. M.A. Abramowicz, V. Karas, W. Kluzniak, W.H. Lee, P. Rebusco, Publ. Astron. Soc. Jpn. **55**, 466 (2003). arXiv:astro-ph/0302183
81. J. Horak, V. Karas, Astron. Astrophys. **451**, 377 (2006). arXiv:astro-ph/0601053
82. I. Banerjee, JCAP **08**, 034 (2022)
83. A.A. Araujo Filho, J.R. Nascimento, A.Yu. Petrov, P.J. Porfírio, Phys. Rev. D **108**, 085010 (2023)
84. S.K. Jha, H. Barman, A. Rahaman, JCAP **04**, 036 (2021)